Chemical Science

ROYAL SOCIETY OF CHEMISTRY

EDGE ARTICLE

View Article Online
View Journal | View Issue

Cite this: *Chem. Sci.*, 2024, **15**, 18431

All publication charges for this article have been paid for by the Royal Society of Chemistry

Received 15th August 2024
Accepted 19th September 2024

DOI: 10.1039/d4sc05494f

rsc.li/chemical-science

Facilitating intrinsic delayed fluorescence of conjugated emitters by inter-chromophore interaction†

Yixuan Gao,‡[a] Yingman Sun,‡[b] Zilong Guo,[a] Guo Yu,[a] Yaxin Wang,[a] Yan Wan,[c] Yandong Han,[d] Wensheng Yang,[d] Dongbing Zhao *[b] and Xiaonan Ma *[a]

Delayed fluorescence (DF) is a unique emitting phenomenon of great interest for important applications in organic optoelectronics. In general, DF requires well-separated frontier orbitals, inherently corresponding to charge transfer (CT)-type emitters. However, facilitating intrinsic DF for local excited (LE)-type conjugated emitters remains very challenging. Aiming to overcome this obstacle, we demonstrate a new molecular design strategy with a DF-inactive B,N-multiple resonance (MR) emitter as a model system. Without the necessity of doping with heavy atoms, we synthesized a co-facial dimer in which an excimer-like state (S_{exc}) was expected to facilitate efficient reverse intersystem crossing (RISC, $T_1 \rightarrow S_{exc}$) and intrinsic DF. Benefiting from greatly enhanced SOC and reduced ΔE_{ST}, the proof-of-concept emitter Np-2CzB exhibited k_{RISC} up to 6.5 $\times$ 10^5 s^{-1} and intrinsic DF with >35% contribution (Φ_{DF}/Φ_F) in dilute solution. Further investigation indicated that S_{exc} state formation relies on an optimized co-facial distance (d = ~4.7 Å), strong inter-chromophore interaction (J_{coul} > 450 cm^{-1}) and a rigid structure ($\Gamma_{S_1 \rightarrow S_0}$ < 350 cm^{-1}). Although our strategy was demonstrated with a B,N-MR emitter, it can be applicable to many LE-type conjugated emitters without intrinsic DF. By triggering potential DF emission, many classic emitters might play a more important role in optoelectronics.

Introduction

The thermally activated delayed fluorescence (TADF) of organic emitters refers to long-lived fluorescent emission occurring with a lifetime similar to phosphorescence, which is usually facilitated by efficient reverse intersystem crossing (RISC) from a populated triplet to a fluorescent singlet state.[1–3] In the area of photophysics, TADF is actually a rather traditional concept. For instance, the unusually strong DF of C_{70} was successfully observed under appropriate conditions,[4] while the DF of Cy-5 dye was demonstrated to be feasible with remarkable back isomerization of the T_1 state.[5] Benefitting from the pioneering work of Adachi *et al.*, TADF emitters received intensive attention for application in the development of electroluminescent devices.[6–8]

In devices, the recombination of injected electrons and holes creates 25% singlet and 75% triplet excitons, in which the TADF mechanism is a feasible way of harvesting generated dark triplet excitons.[9,10] For organic light-emitting diode (OLED) devices, efficient triplet harvesting is regarded as a primary factor for achieving qualified external quantum efficiency (η_{EQE}), which can usually be expressed as a product of several contributing terms:[11,12]

$$\eta_{EQE} = \gamma \times \eta_{EUE} \times \Phi_F \times \eta_{out} \quad (1)$$

in which the exciton utilizing efficiency (η_{EUE}) is directly determined by the efficient harvesting of triplet excitons. Furthermore, organic emitters featuring TADF emission have been demonstrated to be beneficial for pursuing electrically pumped organic lasers (EPOLs), as efficient RISC can greatly release the accumulation of dark triplet excitons, which are not capable of producing stimulated emission in most cases.[13–16] In addition to application to OLEDs and EPOLs, TADF emission has received attention in the area of bio-imaging.[17–20] By using DF emission, time-gated imaging can inherently eliminate interference from short-lived endogenous fluorescence and scattered light, which is very helpful for improving the accuracy and S/N ratio of imaging on a cellular level.[21,22]

However, for the majority of organic emitters, acquiring TADF emission remains challenging. In order to convert a T_1

[a]*Institute of Molecular Plus, Tianjin University, Tianjin 300072, P. R. China. E-mail: xiaonanma@tju.edu.cn*

[b]*State Key Laboratory and Institute of Elemento-Organic Chemistry, College of Chemistry, Nankai University, Tianjin 300071, P. R. China. E-mail: dongbing.chem@nankai.edu.cn*

[c]*College of Chemistry, Beijing Normal University, Beijing 100875, P. R. China*

[d]*Engineering Research Center for Nanomaterials, Henan University, Kaifeng 475004, P. R. China*

† Electronic supplementary information (ESI) available. See DOI: https://doi.org/10.1039/d4sc05494f

‡ These authors contributed equally to this work.

population to the S_1 state, the RISC transition should be fast enough to compete kinetically with radiative and non-radiative $T_1 \rightarrow S_0$ decay.[23–26] According to Fermi's golden rule, the RISC rate (k_{RISC}) is related to spin–orbit coupling (SOC) matrix elements and the S_1–T_1 energy gap (ΔE_{ST}):[2,27,28]

$$k_{RISC} \propto \left| \frac{\left\langle \Psi_{T_1} \middle| \hat{H}_{SO} \middle| \Psi_{S_1} \right\rangle}{\Delta E_{ST}} \right|^2 \quad (2)$$

For the charge-transfer (CT)-type emitters, a minimized ΔE_{ST} is induced by well-separated frontier orbitals (FOs) between electron donor and acceptor.[29–31] Meanwhile, the local-excited (LE) nature of the low-lying triplet states leads to greatly different electronic configurations of the initial and final states of the RISC transition.[32–35] As the result, a moderate SOC, *i.e.* $\langle \Psi_{T_1} | \hat{H}_{SO} | \Psi_{S_1} \rangle$, can be guaranteed. Combining the minimized ΔE_{ST} and moderate SOC, k_{RISC} of 10^4–10^6 s^{-1} can be reached for CT-type TADF emitters.[6,36,37] Although CT-type emitters usually exhibit TADF with a several orders of magnitude slower decay rate (k_{DF}, 10^3–10^5 s^{-1}) than prompt fluorescence (k_{PF}, 10^7–10^9 s^{-1}), the corresponding k_{RISC} can still ensure a maximized η_{EUE} (up to ~100%) in OLED devices.[38–40]

However, for organic emitters with the S_1 state dominated by LE ($\pi \rightarrow \pi^*$) excitation, *i.e.* most conjugated emitters with a rigid polycyclic aromatic framework, an efficient RISC transition is usually inherently blocked. Firstly, the SOC Hamiltonian can be approximately described as:[41,42]

$$\hat{H}_{SO} \approx \sum_i^{N_e} \zeta(r_i) \hat{\mu}_L \hat{\mu}_S \quad (3)$$

For conjugated aromatic emitters, both S_1 and T_1 states are dominated by identical ($\pi \rightarrow \pi^*$) electronic configurations, leading to a near-zero magnetic moment resulting from orbital angular momentum (μ_L) and subsequent weak SOC.[43–45] Moreover, the LE nature of the S_1 state leads to a considerable overlap integral of the FOs, resulting in a large ΔE_{ST}. Therefore, for most conjugated emitters, intrinsic TADF is difficult to achieve.

For instance, with typical conjugated frameworks, multiple resonance (MR) emitters have received enormous attention since the first report by Hatakeyama *et al.* in 2016.[46–50] As B,N-doped conjugated chromophores, B,N-MR emitters exhibit an LE-type ($\pi \rightarrow \pi^*$) S_1 state and low-frequency mode dominated vibronic coupling, leading to a high fluorescence quantum yield (Φ_F) and color purity.[51–54] However, many reported B,N-MR emitters were recognized as TADF-inactive in dilute solution ($k_{RISC} = 10^3$–10^4 s^{-1}) due to weak SOC and large ΔE_{ST}, leading to a nearly negligible contribution from intrinsic TADF, *i.e.* Φ_{DF}/Φ_F < 5%.[46,55,56] Plenty of efforts have been made to overcome the inherent barrier, such as heavy atom (S, Se, *etc.*) doping[57–59] and long-range CT mixing in the S_1 state, by which the k_{RISC} of B,N-MR emitters were promoted to 10^5–10^6 s^{-1}.[60]

On the other hand, it was found that the RISC of many TADF-inactive B,N-MR emitters can be greatly boosted in doped films with a specific host, such as DABNA-1 in mCBP and TBN-TPA in 2,6-DCzppy.[46,61] The underlying mechanism for this intriguing phenomenon was successfully uncovered by Chou and co-workers.[62] In doped films, the S_1 state of B,N-MR emitters can form an exciplex-like state with the host. As a result, the greatly changed electronic configuration of the emitting state (exciplex) leads to enhanced SOC, while ΔE_{ST} can be accordingly reduced as the exciplex is energetically lower than the S_1 state. The landmark work of Chou *et al.* greatly inspired us to explore a new strategy for facilitating the intrinsic TADF of conjugated emitters. As an analog of the guest–host interaction, the intramolecular excimer-like state facilitated by delicate inter-chromophore interaction might lead to similarly enhanced SOC and reduced ΔE_{ST}, resulting in greatly boosted k_{RISC} without the presence of a specific host, *i.e.* intrinsic TADF. More importantly, as a host is no longer included, this strategy may be useful for many conjugated emitters in addition to specific types of emitters. It is worth noting that the strategy of inter-chromophore interaction has been employed to improve the η_{EQE} of small-molecule (first-generation) OLED by the formation of excimer-like states,[63–65] while controllable inter-chromophore interaction by rational molecular design has recently been used for emission switching that can rapidly respond to external stimuli in aggregated states.[66] However, to the best of our knowledge, intrinsic TADF enabled by inter-chromophore interaction has rarely been reported.

In this work, we demonstrate a new strategy for facilitating the intrinsic TADF of conjugated emitters by inter-chromophore interaction. With a TADF-inactive B,N-MR emitter (CzB) as a model system, CzB dimers (BiPh-2CzB and Np-2CzB) with different linkers were synthesized. The fs-TA spectra indicated the formation of an excimer-like state ($S_1 \rightarrow S_{exc}$, ~250 ps) in the S_1 state decay of a proof-of-concept emitter Np-2CzB, leading to efficient RISC ($T_1 \rightarrow S_{exc}$) with k_{RISC} up to 6.5×10^5 s^{-1} and intrinsic TADF with Φ_{DF}/Φ_F > 35% in dilute solution (10^{-5} M). Further investigation indicated that the S_{exc} formation of Np-2CzB is associated with at least three factors: (1) a suitable inter-chromophore distance (d = ~4.7 Å); (2) strong electronic coupling for excimer formation (J_{coul} > 450 cm^{-1}); and (3) a rigid co-facial geometry ($\Gamma_{S1\rightarrow S0}$ < 350 cm^{-1}). The formed S_{exc} state leads to a nearly degenerate S_{exc}/T_1 state (ΔE_{ST} < 20 meV) and enhanced SOC due to the very different electronic configurations of the S_{exc} state, which all contribute to the intrinsic TADF of the proof-of-concept emitter Np-2CzB. Please note that the strategy described in this work should not be limited to B,N-MR emitters. In terms of the underlying photophysics, it can be generalized to any organic conjugated emitters with an S_1 state dominated by LE ($\pi \rightarrow \pi^*$) excitation.

Results and discussion

Molecular design

Here we aim to develop a new strategy which can potentially facilitate the intrinsic TADF of conjugated emitters by inter-chromophore interaction and the corresponding formed excimer-like state (S_{exc}). We selected the B,N-MR emitter CzB, *i.e.* 2,6-bis(3,6-di-*tert*-butyl-9*H*-carbazol-9-yl)boron, as a model chromophore, which was demonstrated to be lacking intrinsic TADF in solution (k_{RISC} = ~1.5×10^4 s^{-1}).[67,68] It is well known that an excimer can usually form between chromophores with co-facial geometry, while the co-facial distance (d) might be the

primary factor for the formation of an S_{exc} state.[69–72] Therefore, we designed two co-facial CzB dimers with different linkers. Please note that dimerization of B,N-MR frameworks has been widely employed in co-planar geometry to extend conjugation and in a helicene structure for chiroptical responses,[73–75] but co-facial dimerization of B,N-MR emitters to facilitate an S_{exc} state has rarely been reported.

As shown in Scheme 1, we employed biphenyl (Biph) and naphthalene (Np) as covalent linkers to construct co-facial CzB dimers with different co-facial distances (d). By using Suzuki coupling (ESI, Section S1†), CzB units were covalently linked to neighboring α sites of Biph and Np linkers, leading to dimers named Biph-2CzB and Np-2CzB, respectively. Preliminary DFT calculation confirmed the co-facial geometry of two CzB units in both Biph-2CzB and Np-2CzB (Table S1†). The co-facial distance (d_{B-B}) in the S_0 state was estimated to be 5.4 Å and 4.9 Å in Biph-2CzB and Np-2CzB, respectively, which are significantly larger than the corresponding distance between neighboring α sites on Biph (3.9 Å) and Np (3.6 Å) due to the non-parallel configuration of the two CzB units. The key role of geometry in inter-chromophore interaction will be discussed in the following sections.

Delayed fluorescence

The steady-state UV/Vis absorption and fluorescence spectra of synthesized CzB, Biph-2CzB and Np-2CzB were measured in N_2-saturated DCM solution (10^{-5} M) and PMMA doped films (0.2 mg g^{-1}). As shown in Fig. 1a and b, Biph-2CzB exhibited fluorescence emission at 500 nm, which is nearly identical to the measured emission spectra of CzB, indicating the absence of inter-chromophore interaction in Biph-2CzB. Meanwhile, an extra-broad emission peak centered at 540 nm was observed for Np-2CzB (Fig. 1c), overlapping with CzB monomer emission at 500 nm. By measuring the concentration-dependent absorption spectra (Fig. S5†) and solvent-polarity-dependent fluorescence spectra (Fig. S6†) of Np-2CzB, the participation of inter-molecular interaction and long-range CT states can be ruled out. Thus, the observed broad emission of Np-2CzB at 540 nm was preliminarily assigned to the emission of the expected S_{exc} state. We further examined the potential TADF activity of synthesized CzB, Biph-2CzB and Np-2CzB emitters. By measuring the fluorescence spectra in air- (triplet states are quenched) and N_2-saturated DCM solution, both CzB (Fig. 1d) and Biph-2CzB (Fig. 1e) were recognized as TADF inactive. However, pronounced TADF was observed for Np-2CzB (Fig. 1f), and the fluorescence spectra in N_2-saturated solution were substantially stronger than in an air-saturated solution. Intriguingly, the observed TADF (green line in Fig. 1f) exhibited a single peak at 540 nm, different from the double-peak shape (500 nm and 540 nm) of the fluorescence spectra of Np-2CzB, indicating that TADF is associated only with the S_{exc} state.

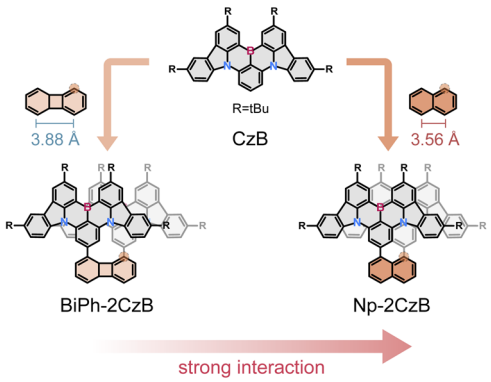

Scheme 1 Molecular design of co-facial CzB dimers with biphenylene (BiPh) and naphthalene (Np) as covalent linkers.

To quantify the contributions of the PF and DF components, we estimated the total fluorescence quantum yield (Φ_F) and the contributions of PF and DF components, *i.e.* Φ_{PF}, Φ_{DF} and $\Phi_F = \Phi_{PF} + \Phi_{DF}$. As shown in Fig. 1g–i and Table 1, CzB exhibits a Φ_F of ~100% with a low DF contribution in both DCM solution ($\Phi_{DF}/\Phi_F = 0.11$) and PMMA doped films ($\Phi_{DF}/\Phi_F = 0.01$), which is consistent with the typical LE ($\pi \rightarrow \pi^*$) character of the S_1 state.[76–78] Furthermore, although Biph-2CzB is much less fluorescent ($\Phi_F < 0.5$) than CzB, its DF contributions in DCM solution ($\Phi_{DF}/\Phi_F = 0.10$) and PMMA doped films ($\Phi_{DF}/\Phi_F = 0.02$) are very consistent with the corresponding values for CzB, indicating similar RISC and different S_1 state relaxation channels, such as faster non-radiative decay and slower radiative decay of Biph-2CzB compared with CzB. Intriguingly, Np-2CzB exhibited a considerable DF contribution ($\Phi_{DF}/\Phi_F = 0.37$) in DCM solution, indicating an efficient RISC channel predominantly associated with S_{exc} emission at 540 nm. We further measured the fluorescence decay traces of CzB, Biph-2CzB and Np-2CzB in DCM solution (Fig. 2) and PMMA doped films (Fig. S7†) to investigate the relaxation channels of the corresponding low-lying singlet and triplet states. As shown in Fig. 2a, CzB exhibited a PF lifetime of $\tau_{PF} = 6.30$ ns and a barely observable DF component in DCM solution, which is comparable with the measured $\tau_{PF} = 9.00$ ns of Biph-2CzB. Although a long-lived tail can be observed in the fluorescence decay traces of CzB and Biph-2CzB in DCM solution, its low contribution (<10 photon counts compared with 10^4 counts at the maximum) resulted in difficulty in the quantitative fitting of τ_{DF}. Thus, the lack of intrinsic TADF was confirmed for CzB and Biph-2CzB, corresponding to the reported slow RISC of CzB ($k_{RISC} = 1.5 \times 10^4$ s^{-1}) in solution.[67,68]

However, as shown in Fig. 2b, Np-2CzB exhibited bi-exponential fluorescence decay in DCM solution ($\tau_{PF1} = 5.6$ ns and $\tau_{PF2} = 49.4$ ns) and PMMA doped films ($\tau_{PF1} = 5.2$ ns and $\tau_{PF2} = 49.1$ ns). More specifically, emission at 500 nm is dominated by fast decay ($\tau_{PF1} = \sim 5.6$ ns), assigned to the S_1 state lifetime, which is consistent with the measured τ_{PF} of CzB and Biph-2CzB. Meanwhile, slow decay ($\tau_{PF2} = \sim 49$ ns) is associated with S_{exc} at 540 nm, which agrees with the prolonged lifetime of the excimer-like states in reported cases.[79–82]

Please note that the observed τ_{PF2} must be distinguished from the TADF of Np-2CzB, which was observed with a lifetime of ~2.5 μs (τ_{DF}, Fig. 2c) in DCM solution and is associated with S_{exc} emission at 540 nm. With the measured fluorescence quantum yield (Φ_{PF}, Φ_{DF}) and lifetime (τ_{PF}, τ_{DF}), we calculated the decay rate of each relaxation channel (ESI, Section S2†), *i.e.*

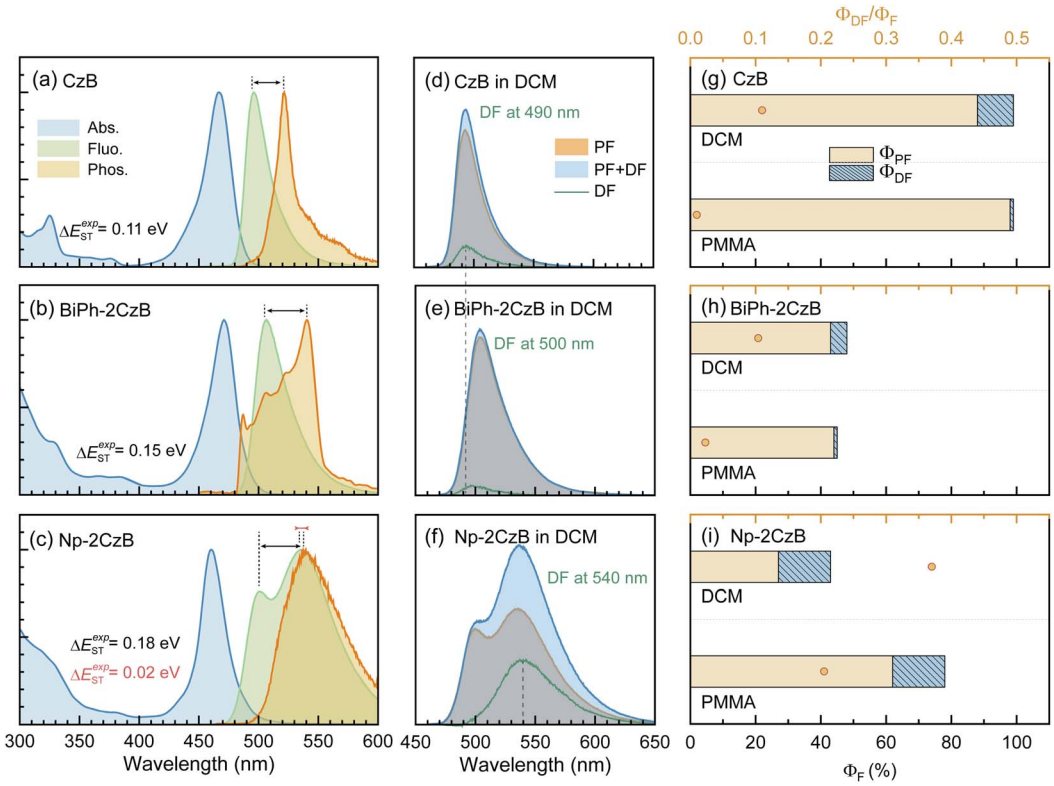

Fig. 1 Measured absorption, fluorescence and phosphorescence (50 ms gated) spectra of CzB (a), BiPh-2CzB (b) and Np-2CzB (c) in N_2-saturated DCM solution (1×10^{-5} M); comparison of fluorescence spectra of CzB (d), BiPh-2CzB (e) and Np-2CzB (f) in air- (gray bands) and N_2- (blue bands) saturated DCM solution (1×10^{-5} M), the differential spectra (green lines) correspond to the DF component, measured fluorescence quantum yield (Φ_F, Φ_{PF}, Φ_{DF}) and relative contribution of delayed fluorescence (Φ_{DF}/Φ_F) of CzB (g), BiPh-2CzB (h) and Np-2CzB (i) in N_2-saturated DCM solution (1×10^{-5} M) and PMMA doped films (0.2 mg g^{-1}).

k_r^S, k_{nr}^S, k_{ISC} and k_{RISC}. As listed in Table 1, CzB exhibits highly efficient radiative decay to the S_0 state ($k_r^S = 1.4 \times 10^8$ s^{-1}), which is one or two orders of magnitude faster than the corresponding k_{nr}^S and k_{ISC}, leading to close-to-unity Φ_F. Please note that we can barely observe the DF components of CzB and Biph-2CzB in DCM solution (Fig. 2a), for which k_{RISC} cannot be calculated. However, a k_{RISC} of 1.5×10^4 s^{-1} was reported for CzB in dilute solution,[67,68] which is half of our measured value ($k_{RISC} = 2.9 \times 10^4$ s^{-1}) of CzB in PMMA doped films. Meanwhile, Biph-2CzB exhibited very similar RISC dynamics to CzB, *i.e.* unobservable RISC in DCM solution and $k_{RISC} = 4.9 \times 10^4$ s^{-1} in PMMA doped films. However, unlike CzB, the k_{nr}^S value ($\sim 5.2 \times 10^7$ s^{-1} in DCM solution) of Biph-2CzB was fast enough to be competitive with k_r^S ($\sim 4.8 \times 10^7$ s^{-1} in DCM solution), leading to $\Phi_F < 0.5$. Since the band gaps of CzB and Biph-CzB are similar to each other, the observation that the k_{nr}^S of Biph-CzB is nearly 50 times faster than that of CzB might be attributed to specific vibrational modes with a pronounced Huang–Rhys factor (S_k) and reorganization energy contribution (λ_k) to the $S_1 \rightarrow S_0$

Table 1 Photophysical parameters of CzB, BiPh-2CzB and Np-2CzB measured in DCM solution and PMMA doped films

		Φ_{PF}	Φ_{DF}	τ_{PF} (ns)	τ_{DF} (μs)	k_r^{Sa} (10^7 s^{-1})	$k_{nr}^{S\,b}$ (10^6 s^{-1})	$k_{ISC}{}^c$ (10^6 s^{-1})	$k_{RISC}{}^d$ (10^5 s^{-1})
CzB	DCM	0.88	0.11	6.30	—	14.0	1.41	17.6	0.15[e]
	PMMA	0.98	0.01	6.80	35.2	14.4	1.46	1.49	0.29
BiPh-2CzB	DCM	0.43	0.05	9.00	—	4.78	51.8	11.6	—
	PMMA	0.44	0.01	9.90	20.6	4.40	53.8	2.22	0.49
Np-2CzB	DCM	0.27	0.16	5.60[f] 49.4[g]	2.50	0.55	7.25	7.53	6.45
	PMMA	0.62	0.16	5.20[f] 49.1[g]	1.25	1.26	3.56	4.18	1.01

[a] Calculated with $k_r^S = \Phi_{PF}/\tau_{PF}$. [b] Calculated with $k_{nr}^S = k_{PF} - k_r^S - k_{ISC}$, $k_{PF} = 1/\tau_{PF}$. [c] Calculated with $k_{ISC} = k_{PF}\Phi_{ISC} = k_{PF} \times \Phi_{DF}/\Phi_F$. [d] Calculated with $k_{RISC} = (k_{PF} + k_{DF})/2 - [(k_{PF} + k_{DF})^2/2 - k_{PF}k_{DF}(1 + \Phi_{DF}/\Phi_{PF})]^{0.5}$. [e] Collected from values reported in ref. 64. [f] τ_{PF} of S_1 state, *i.e.* CzB monomers in Np-2CzB. [g] τ_{PF} of S_{exc} state.

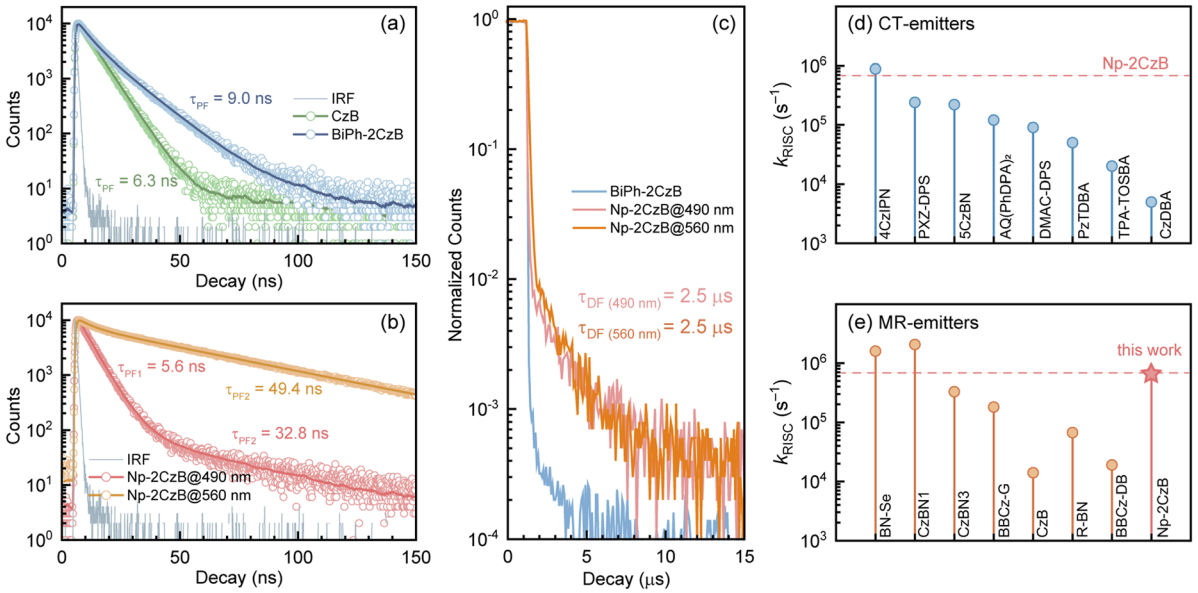

Fig. 2 (a) The PF decay traces of CzB and Biph-2CzB in DCM solution; (b) the PF decay traces of Np-2CzB at emission wavelengths of 490 nm and 560 nm in DCM solution; (c) the DF decay traces of Biph-2CzB and Np-2CzB in DCM solution, in which the DF component of Biph-2CzB was unobservable; (d) reported k_{RISC} values of several typical CT-type TADF emitters in dilute solution; (e) comparison between the measured k_{RISC} value of our proof-of-concept emitter Np-2CzB with several reported B,N-MR emitters in dilute solution.

transition, which was described as the band-gap law in a weak coupling regime.[24,25,31]

Furthermore, the observed DF contribution ($\Phi_{DF}/\Phi_F = 0.37$) and ~2.5 μs DF lifetime of Np-2CzB correspond to a surprisingly high $k_{RISC} = 6.5 \times 10^5\ s^{-1}$ in DCM solution. Quantitatively, the estimated $k_{RISC} = 6.5 \times 10^5\ s^{-1}$ in DCM solution is nearly 50 times faster than the reported k_{RISC} of CzB ($1.5 \times 10^4\ s^{-1}$), which is also comparable to reported selenium-doped B,N-MR emitters with symmetric (BN–SeSe, $k_{RISC} = 2.0 \times 10^6\ s^{-1}$) and asymmetric (BN–Se, $k_{RISC} = 1.6 \times 10^6\ s^{-1}$) frameworks.[57,59] As illustrated in Fig. 2d and e, the measured k_{RISC} of Np-2CzB is higher than those of many well-known CT-type TADF emitters and recently reported B,N-MR emitters in dilute solution; the details can be found in Tables S2 and S3.†

We then attempted to explore the plausible origin of the efficient RISC of Np-2CzB in dilute solution. As described in eqn (2), k_{RISC} is highly dependent on ΔE_{ST} and the corresponding SOC matrix element $\langle \Psi_{T_1} | \hat{H}_{SO} | \Psi_{S_1} \rangle$.[28,43,83] To estimate ΔE_{ST}, we measured the phosphorescence spectra of CzB, Biph-2CzB and Np-2CzB in DCM solution at 77 K (Fig. 1a–c), in which the PF component was screened by 50 ms time-gating. Combined with the corresponding fluorescence spectra, ΔE_{ST} of 0.11 eV (CzB) and 0.17 eV (Biph-2CzB) were estimated, which are much smaller than the TDDFT calculated values (Fig. S8†) and usually regarded as a thermally accessible gap at room temperature.[37,84] Therefore, the RISC channels of CzB and Biph-2CzB might be mainly blocked by a low SOC matrix element, and were calculated as 0.044 cm^{-1} and 0.005 cm^{-1}, respectively, using the linear-response method. As both S_1 and T_1 states of CzB feature an identical LE ($\pi \rightarrow \pi^*$) electronic configuration, the magnetic moment resulting from orbital angular momentum (μ_L) can be extremely low, leading to the TADF-inactive character of CzB and Biph-2CzB. For Np-2CzB, although $\langle \Psi_{T_1} | \hat{H}_{SO} | \Psi_{S_1} \rangle$ was also calculated to be low (<0.1 cm^{-1}), the $\langle \Psi_{T_1} | \hat{H}_{SO} | \Psi_{S_{exc}} \rangle$ associated with RISC ($T_1 \rightarrow S_{exc}$) can be much higher due to the dramatically changed electronic configuration of the S_{exc} state, which explains the observed fact that the TADF of Np-2CzB is associated only with S_{exc} emission. Due to the limitation of electronic structure calculation of an excimer-like state, directly calculating the SOC matrix element involving the S_{exc} state remains challenging, but we still believe that the greatly enhanced SOC may be the main reason for the intrinsic TADF of Np-2CzB. Meanwhile, as the S_{exc} state is energetically lower than the S_1 state of Np-2CzB, the resulting ΔE_{ST} ($T_1 \rightarrow S_{exc}$) < 0.02 eV may also contribute to the observed k_{RISC} of $6.5 \times 10^5\ s^{-1}$ in DCM solution.

Inter-chromophore interaction

We successfully observed the intrinsic TADF of Np-2CzB, which is associated with the S_{exc} state facilitated by inter-chromophore interaction. The formation of the S_{exc} state relies on interaction between a chromophore (M*) with a localized S_1 state and the neighboring chromophore (M) on the S_0 state, *i.e.* $|^1(S_1S_0)\rangle = (1/2)^{0.5}[|M^*M\rangle \pm |MM^*\rangle]$.[85,86] For Np-2CzB, the formed S_{exc} state exhibited red-shifted emission and efficient RISC ($k_{RISC} = 6.5 \times 10^5\ s^{-1}$) in DCM solution. However, Biph-2CzB exhibited nearly identical emission to CzB, indicating very weak inter-chromophore interaction. We performed reduced density gradient (RDG) analysis for Biph-2CzB and Np-2CzB (Fig. 3a and b).

The calculated RDG scattering diagram of Np-2CzB exhibited several spikes in the low-density and low-gradient region (highlighted by the dashed box in Fig. 3b), indicating the

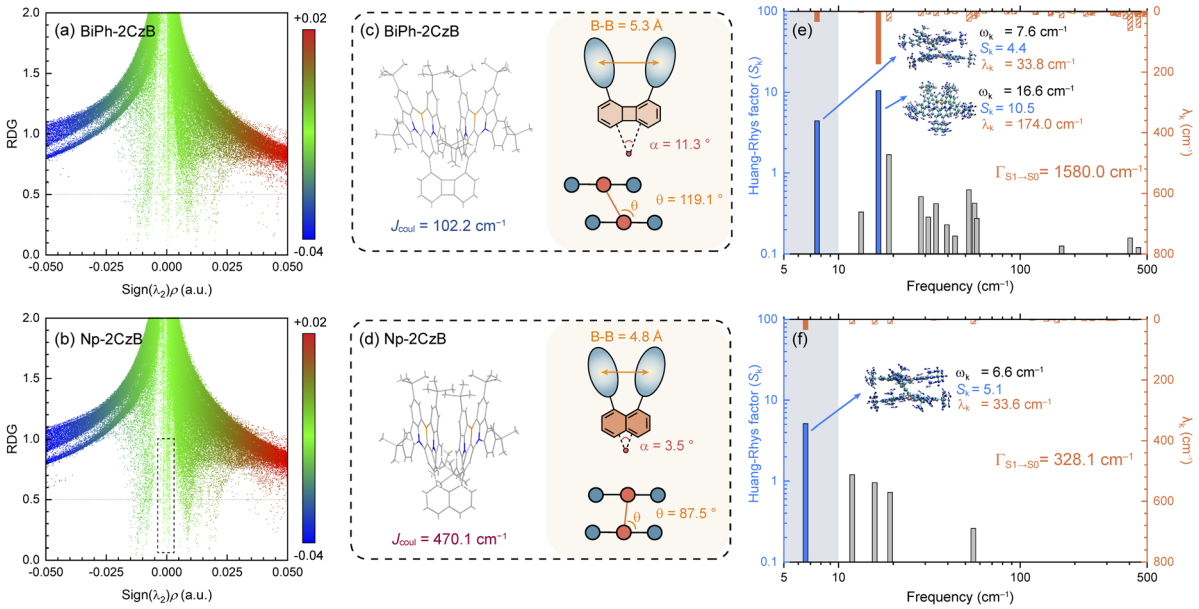

Fig. 3 Calculated reduced density gradient (RDG) scattering diagrams based on the S_1 state geometry of BiPh-2CzB (a) and Np-2CzB (b); the TDDFT (B3LYP/6-31g*) optimized geometry of BiPh-2CzB (c) and Np-2CzB (d); calculated Huang–Rhys factor (S_k) and reorganization energy contribution (λ_k) of each vibrational mode of BiPh-2CzB (e) and Np-2CzB (f) for the $S_1 \rightarrow S_0$ transition.

presence of pronounced inter-chromophore interaction, which can also be visualized by the corresponding RDG iso-surface displayed in Fig. S9.† However, such features can barely be observed on the RDG scattering diagram and iso-surface of Biph-2CzB, implying the absence of inter-chromophore interaction, which is consistent with its observed fluorescence spectra being similar to CzB. We further attempted to explore the structural and energetic origin of the different inter-chromophore interactions within the two CzB dimers with different linkers.

Firstly, S_{exc} formation relies on co-facial geometry with a suitable co-facial distance (d = 3.0–5.0 Å),[87–89] for which we optimized the S_1 state structure of BiPh-2CzB and Np-2CzB by the TDDFT approach; the corresponding structural parameters are listed in Table 2. As illustrated in Fig. 3c and d, Np-2CzB exhibited a co-facial (B–B) distance of d = 4.8 Å in the S_1 state, which is 0.5 Å shorter than that of BiPh-2CzB (d = 5.3 Å). Meanwhile, the S_1 state geometry of Np-2CzB exhibited a dihedral angle of $\alpha = 3.5°$ and a slipping angle of $\theta = 87.5°$ between the two CzB units. As a result, Np-2CzB exhibited improved co-facial configuration in the S_1 state compared to BiPh-2CzB (α = 11.3°, θ = 119.1°), *i.e.* the two CzB units are more spatially overlapped in Np-2CzB than in BiPh-2CzB, leading to a favorable configuration for S_{exc} formation. Furthermore, the calculated S_0 and S_1 state geometries also revealed the different S_1/S_0 excited-state structural relaxation (ES-SR) of BiPh-2CzB and Np-2CzB. As listed in Table 2, BiPh-2CzB exhibited pronounced CzB twisting (β_1/β_2) and bending (γ_1/γ_2) angles with up to 30% change between S_1 and S_0 states, which might lead to two-step S_1/S_0 ES-SR, as we reported previously.[31,55] Intriguingly, the twisted S_1/S_0 ES-SR of Np-2CzB (~7% S_1/S_0 changing) is less pronounced than that of BiPh-2CzB. Meanwhile, the two CzB units in Np-2CzB exhibited a significantly planarized (bending angles $\gamma_1/\gamma_2 = 5.1°$) feature in the S_1 state compared to CzB (γ = 18.5°) or BiPh-2CzB (γ_1/γ_2 = 11.3°/15.7°), which might also contribute to the S_{exc} state formation of Np-2CzB. Furthermore, the formation of an S_{exc} state also relies on appreciable inter-chromophore electronic coupling (J), which has been widely discussed in the framework of the exciton theory.[90–92] In general, electronic coupling includes contributions from Coulomb (J_{coul}) and charge transfer terms (J_{CT}), while S_{exc} state formation is known to require considerable J_{coul} and weak CT coupling.[70,93] The low value of J_{CT} in both BiPh-2CzB and Np-2CzB can be

Table 2 The DFT/TDDFT calculated geometric parameters, electronic coupling (J_{coul}) and reorganization energy ($\Gamma_{S_1 \rightarrow S_0}$ and $\Gamma_{S_0 \rightarrow S_1}$) of CzB, BiPh-2CzB and Np-2CzB

	BiPh-2CzB		Np-2CzB		CzB	
	S_0	S_1	S_0	S_1	S_0	S_1
α (°)[a]	11.2	11.3	4.8	3.5		
θ (°)[b]	118.5	119.1	91.3	87.5		
J_{coul} (cm^{-1})	102.2		470.1			
B–B (Å)[c]	5.4	5.3	4.9	4.8		
N_1–N_1 (Å)[c]	5.2	5.1	4.7	4.7		
N_2–N_2 (Å)[c]	5.2	5.1	4.7	4.7		
β_1/β_2 (°)[d]	41.7/45.6	30.0/31.9	52.1/52.1	48.4/48.4		
γ_1/γ_2 (°)[e]	16.6/13.7	11.3/15.7	9.3/9.3	5.1/5.1	19.9	18.5
$\Gamma_{S_1 \rightarrow S_0}$ (cm^{-1})	1579.9		328.1		480.6	
$\Gamma_{S_0 \rightarrow S_1}$ (cm^{-1})	1661.8		423.2		410.4	

[a] Dihedral angle between two CzB units. [b] Slipping angle of two CzB units. [c] Distance between two CzB units. [d] Twisting angle of two CzB units with BiPh/Np linker. [e] Bending angle of two CzB units.

ensured by their barely observable solvatochromism (Fig. S6†), while J_{coul} can usually be estimated with:[85,93,94]

$$J_{coul} = \frac{1}{4\pi\varepsilon_0}\frac{\mu^2(\cos\alpha - 3\cos^2\theta)}{d^3} \quad (4)$$

By using TDDFT calculated geometric parameters (α angle, θ angle and inter-chromophore distance d) and transition dipole moment μ, the inter-chromophore J_{coul} of Np-2CzB was estimated as 470.1 cm^{-1}, which is more than 4.5 times the calculated J_{coul} for Biph-2CzB (102.2 cm^{-1}) and consistent with the reported J_{coul} value for excimer formation in π-stacked dimers of perylene bisimide (PBI), *i.e.* Bis-PBI 1 (J_{coul} = 678.0 cm^{-1}) and Bis-PBI 3(S) (J_{coul} = 545.0 cm^{-1}), in which two PBI chromophores are covalently linked by spacer moieties.[95,96]

Finally, with suitable co-facial geometry and electronic coupling, the formation of the S_{exc} state can still be disrupted by vibrational motion and S_1/S_0 ES-SR of the S_1 state, for which we further performed vibrational analysis on BiPh-2CzB and Np-2CzB. By performing vibrational analysis, we estimated the total internal reorganization energy of the $S_1 \rightarrow S_0$ transition ($\Gamma_{S_1\rightarrow S_0}$), which can be employed to generalize the S_1/S_0 ES-SR. It can be seen that the $\Gamma_{S_1\rightarrow S_0}$ of BiPh-2CzB (1579.9 cm^{-1}) is almost 5 times that of CzB (480.6 cm^{-1}) (Fig. S10†), indicating the highly flexible structure of BiPh-2CzB in the S_1 state, which can potentially disrupt the formation of the S_{exc} state. In contrast, the $\Gamma_{S_1\rightarrow S_0}$ of Np-2CzB (328.1 cm^{-1}) is even lower than that of CzB, indicating a rigid structure without pronounced vibrational motion in the S_1 state, which might also be critical for S_{exc} formation. We further calculated the Huang–Rhys factor (S_k) and reorganization energy contribution (λ_k) of each vibrational mode and attempted to find the key modes that can promote or disrupt S_{exc} formation.

It is known that vibrational modes with considerable S_k (*i.e.* promoting modes) are heavily involved in the vibronic coupling of the S_1 state, while the λ_k of promoting modes is associated with either S_1/S_0 ES-SR or the vibrational motion of the S_1 state,[97–100] which can disrupt S_{exc} formation. As shown in Fig. 3e, the $\Gamma_{S_1\rightarrow S_0}$ of BiPh-2CzB is mainly contributed by two promoting modes in the low-frequency regime, *i.e.* mode 1 (S_k = 4.4) at ω_k = 7.6 cm^{-1} with λ_k = 33.8 cm^{-1} and mode 2 (S_k = 10.5) at ω_k = 16.6 cm^{-1} with λ_k = 174.0 cm^{-1}. As illustrated in Fig. S11,† mode 1 corresponds to the twisting motion of two CzB units along with a Biph linker, associated with the fluctuation of β_1/β_2 and θ angles with respect to the equilibrium position in the S_1 state. Meanwhile, mode 2 corresponds to bending of the CzB units, *i.e.* the fluctuation of γ_1/γ_2 angles. Intriguingly, for Np-2CzB, mode 1 was found to be identical to that of BiPh-2CzB (Fig. 3f), but mode 2 of Np-2CzB at ω_k = 15.8 cm^{-1} was one order of magnitude lower at λ_k (15.1 cm^{-1}) than that of BiPh-2CzB, indicating that the bending motion of CzB units is greatly suppressed in the S_1 state of Np-2CzB. Thus, we deduced that the bending mode (ω_k = ~16 cm^{-1}) of CzB can potentially disrupt S_{exc} formation in co-facial dimers, while reducing the λ_k of such a mode might be critical for formation of the S_{exc} state.

The vibrational analysis can also explain the excitation (λ_{ex})-dependent emission of Np-2CzB in DCM solution (Fig. 4a) and PMMA doped films (Fig. 4b). By performing multi-Gaussian fitting on the emission spectra of Np-2CzB (Fig. S12 and S13†), the contributions of S_1 and S_{exc} state emission can be quantified. For convenience, we defined the indicator $\delta = A_{exc}/A_{S_1}$, in which A_{exc} and A_{S_1} stand for the peak areas of S_{exc} and S_1 emission spectra, respectively. In DCM solution, the δ indicator exhibits pronounced λ_{ex}-dependence, *i.e.* visible excitation (λ_{ex} > 410 nm) resulting in S_{exc} dominated emission (δ > 12), while S_{exc} might be disrupted (δ < 6) upon UV excitation (λ_{ex} < 350 nm). As illustrated in Fig. 4c, the UV excitation populated high-lying singlet states (S_n, n > 1) can rapidly decay to a vibrationally hot S_1 state. As a result, the excessive vibrational energy (probably on the bending mode of CzB units) can disrupt S_{exc} formation, leading to reduced δ values, while a cold S_1 state populated by visible excitation leads to a more favourable condition for S_{exc} formation with reduced vibrational motion in the S_1 state. However, in PMMA doped films, the vibrational motion of the corresponding mode might be greatly confined, leading to λ_{ex}-independent emission. Meanwhile, due to external structural restraint on S_1/S_0 ES-SR, the CzB units in the S_1 state might not be fully relaxed to an optimal configuration (bending angles γ_1/γ_2 = 5.1°) that is favorable for S_{exc} formation. As a result, the S_{exc} emission remains at a low level (δ < 8) upon all tested λ_{ex}. Vibrational analysis and λ_{ex}-dependent emission spectra of Np-2CzB further confirmed that S_{exc} formation in Np-2CzB can be disrupted by the bending mode of CzB units, which is strongly coupled with the $S_1 \rightarrow S_0$ transition. However, the formation dynamics of the S_{exc} state in Np-2CzB still remains unknown, because of which we performed fs-TA measurement on CzB, BiPh-2CzB and Np-2CzB in both DCM solution and PMMA doped films.

Excited-state dynamics

To further resolve the excited-state relaxation of CzB, BiPh-2CzB and Np-2CzB emitters, especially to explore the formation dynamics of the S_{exc} state, the fs-TA response of the corresponding emitters in both DCM solution and PMMA doped films were recorded upon UV excitation.

As shown in Fig. S14,† the fs-TA spectra of CzB exhibited pure decay without reshaping of the fs-TA spectra at a probe wavelength of λ_{pr} = 350–750 nm. With minimized S_1/S_0 ES-SR (Table 2), S_1 state decay is dominated by the radiative channel, leading to close-to-unity Φ_F (Table 1). For BiPh-2CzB, pronounced S_1/S_0 ES-SR leads to highly efficient ($k_{nr}^S \approx 5 \times 10^7$ s^{-1}) non-radiative $S_1 \rightarrow S_0$ decay. However, the fs-TA spectral shape of BiPh-2CzB (Fig. S15†) remains nearly unchanged in a time window up to 7 ns, indicating that fs-TA in the UV/Vis regime is insensitive to S_1/S_0 ES-SR of these emitters. Thus, observation of S_1/S_0 ES-SR dynamics relies on quantitative fitting of fs-TA. Intriguingly, the fs-TA spectra of Np-2CzB exhibit a negative band at λ_{pr} = ~465 nm in both DCM solution and PMMA doped films (Fig. S16†), which is clearly blue shifted in comparison with CzB (λ_{pr} = ~475 nm) and BiPh-2CzB (λ_{pr} = ~478 nm). Considering that the observed negative band is comprised of ground state bleaching (GSB) and stimulated emission (SE) of the S_1 state, the blue-shifted negative fs-TA band of Np-2CzB can be explained by the lack of an SE (S_1)

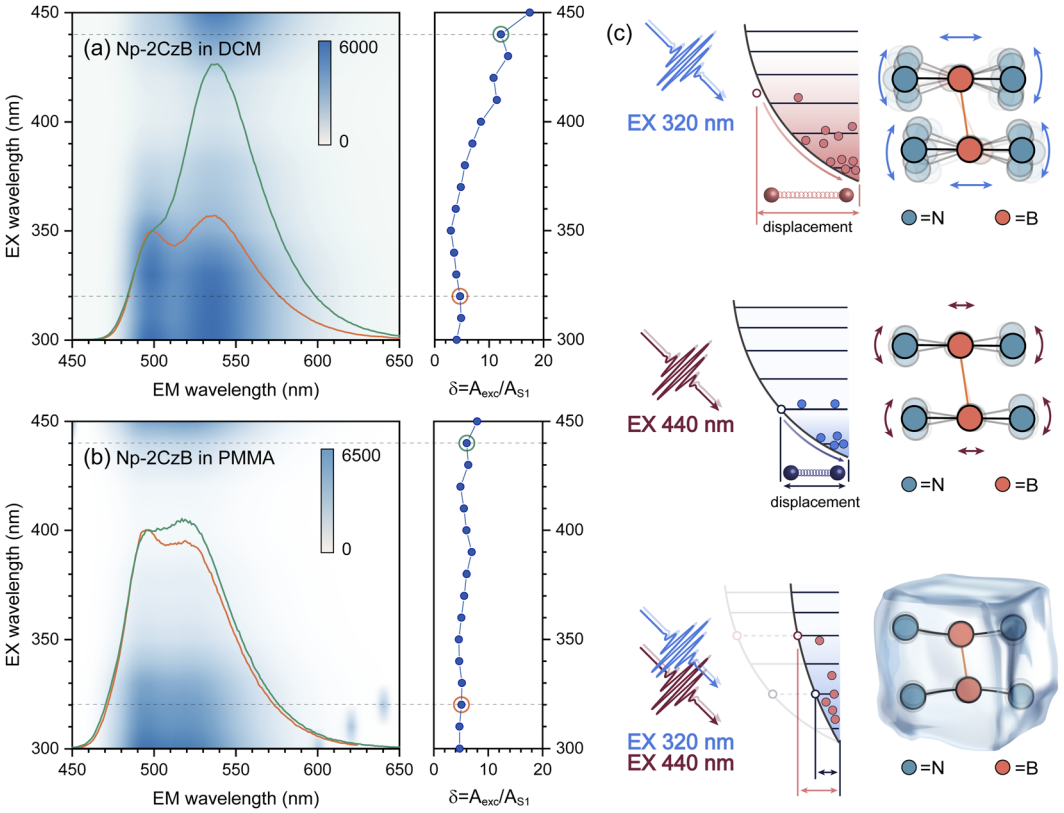

Fig. 4 The measured excitation–emission spectra of Np-2CzB in DCM solution (a) and PMMA doped films (b); corresponding excitation dependence of the contribution ratio (A_{exc}/A_{S_1}) of S_{exc} and S_1 emission, as well as emission spectra upon excitation at 320 nm (orange lines) and 440 nm (green lines); (c) illustrative sketch of S_{exc} emission upon 320 nm (upper) and 440 nm excitation (middle) in solution and in PMMA doped films (bottom).

band, while the replaced S_{exc} state might not be capable of having an SE.

Target analysis was further performed to acquire quantitative information about the excited-state relaxation of BiPh-2CzB and Np-2CzB, in which formation of an S_{exc} state might be entangled with S_1/S_0 ES-SR motion. By including two or three sequential processes, the measured fs-TA data can be well reproduced by the extracted decay-associated spectra (DAS, Fig. 5a–d and S17†) of each decay process and the concentration evolution of each transient species (Fig. 5e, f and S18†).

For CzB, an ultrafast process ($S_1^{FC} \rightarrow S_1^{'}$, τ_1) might correspond to the slight S_1/S_0 ES-SR revealed by TDDFT calculation, which becomes slower (~6.4 ps) in PMMA doped film than in DCM solution (~2.0 ps) due to external structural restraint. The subsequent process (~5 ns) accompanied by the S_1 state SE at ~490 nm corresponds to the S_1 state lifetime ($S_1^{'} \rightarrow S_0$, τ_{S_1}), which is comparable to the measured fluorescence lifetime (τ_{PF}).

For BiPh-2CzB, target analysis revealed two-step relaxation with 2–3 times slower time constants in PMMA doped films than in DCM solution, corresponding to two-step S_1/S_0 ES-SR, as previously reported.[31,55] As discussed in the sections above, S_1/S_0 ES-SR of BiPh-2CzB features simultaneous changing of CzB twisting (β_1 and β_2 angles) and their own bending motion (γ_1 and γ_2 angles). The fast step of S_1/S_0 ES-ER (τ_1 = 1–4 ps) corresponds to CzB twisting along with the biphenyl linker (noted as $S_1^{FC} \rightarrow S_1^{T}$), while the slow step ($\tau_2$ = 150–350 ps) might originate from the bending motion of CzB frameworks ($S_1^{T} \rightarrow S_1^{TB}$). Furthermore, the structurally relaxed S_1 state (S_1^{TB}) exhibits decay with >7 ns time constants, which is comparable to the measured τ_{PF} = 9 ns, corresponding to the S_1 state lifetime (τ_{S_1}). The corresponding DAS of τ_{S_1} feature a pronounced negative peak at λ_{pr} = 475–480 nm, contributed by the GSB and SE of relaxed S_1^{TB}. Meanwhile, the τ_{S_1} of BiPh-2CzB is also similar to the τ_{PF} (~7 ns) of CzB. Therefore, it is clear that the S_1 state of BiPh-2CzB is dominated by CzB units without interchromophore interaction. Since the S_1/T_1 states of CzB units are dominated by similar $\pi \rightarrow \pi^*$ character, the RISC of $T_1 \rightarrow S_1$ is actually forbidden, leading to TADF-inactive Biph-2CzB.

In comparison, Np-2CzB exhibited very different excited-state dynamics. In DCM solution, two-step relaxation of the initially populated S_1^{FC} of Np-2CzB was observed (Fig. 5b). Although the fast step (τ_1 = 2.9 ps) can be assigned to S_1/S_0 CzB twisting ($S_1^{FC} \rightarrow S_1^{'}$), the slow step ($\tau_2$ = 240 ps) can hardly be attributed to S_1/S_0 ES-ER as it became faster (~180 ps) in PMMA doped films. With external structural restraint in doped films, the promoting modes that can disrupt S_{exc} formation, such as the bending mode of CzB units in Np-2CzB, can be further suppressed. As a result, unlike S_1/S_0 ES-ER, S_{exc} formation can be even faster in PMMA doped films than in solution, which is

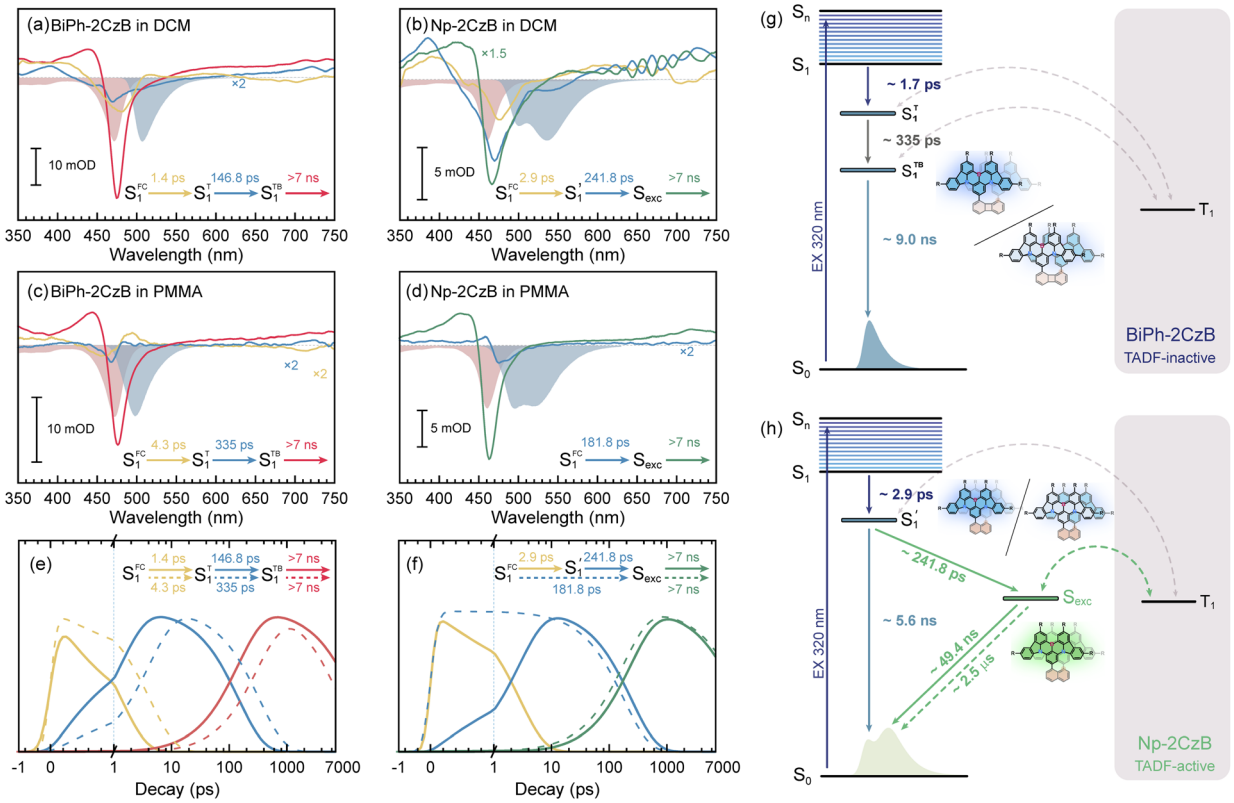

Fig. 5 Target analysis extracted decay-associated spectra (DAS) of fs-TA data of BiPh-2CzB (a) and Np-2CzB (b) in DCM solution, as well as BiPh-2CzB (c) and Np-2CzB (d) in PMMA doped films; the corresponding steady absorption (red filled bands) and fluorescence spectra (blue filled bands) overlap; concentration evolution of transient species extracted from the fs-TA of BiPh-2CzB (e) and Np-2CzB (f) in DCM solution (solid lines) and PMMA doped films (dashed lines); simplified excited-state relaxation path of BiPh-2CzB (g) and Np-2CzB (h).

what we observed for Np-2CzB. Therefore, the observed 180–240 ps process was assigned to the formation of the S_{exc} state ($S_1' \rightarrow S_{exc}$), which is consistent with the reported formation time of an intramolecular excimer of ~250 ps in sandwich-linked dicarbazolyl compounds (*m*-DCzPe) and of ~140 ps in Ant-$(SiMe_2)_n$-Ant, in which two anthracene groups are linked by disilane.[101,102] Meanwhile, it is found that the corresponding DAS of further relaxation of S_{exc} features a negative peak at λ_{pr} = 460–465 nm, *i.e.* ~700 cm^{-1} blue shifted compared to the corresponding peak of Biph-2CzB, which can be explained by the reduced SE (S_1) signal due to the $S_1 \rightarrow S_{exc}$ transition and the lack of SE for the S_{exc} state. Therefore, the observed long-lived species on fs-TA of can be largely attributed to the formed S_{exc} state.

Intriguingly, the S_1/S_0 ES-SR associated with CzB bending motion was missing in the fs-TA of Np-2CzB, which can be explained by two aspects: (1) CzB bending in the S_1 state takes place in a similar timescale to S_{exc} formation, because of which the two parallel processes cannot be distinguished from each other; (2) CzB bending might be too weak to be detected, which is consistent with the low contribution of reorganization energy (λ_k = 15.1 cm^{-1}) of the corresponding vibrational mode at ω_k = 15.8 cm^{-1}. Actually, as discussed above, since the pronounced bending motion of CzB units might be able to disrupt S_{exc} formation, the greatly suppressed bending motion of S_1/S_0 ES-SR might be the key factor for S_{exc} formation in Np-2CzB. On the other hand, please note that although external structural restraint in PMMA doped films leads to the kinetically faster formation of the S_{exc} state, there might be a higher ratio at which Np-2CzB cannot fully relax to the optimized structure of the S_1 state for S_{exc} formation. As a result, we observed a significantly higher DF ratio of Np-2CzB in DCM solution (Φ_{DF}/Φ_F = 0.37) than in PMMA doped films (Φ_{DF}/Φ_F = 0.20).

Unlike Biph-2CzB, the delocalized nature of the S_{exc} state ensures that its electronic configuration is very different from the LE ($\pi \rightarrow \pi^*$) nature of the S_1 and T_1 states, leading to the greatly enhanced $\langle \Psi_{S_{exc}} | \hat{H}_{SO} | \Psi_{T_1} \rangle$ of Np-2CzB. Meanwhile, the nearly degenerate excitation energy of the S_{exc} and T_1 states leads to $\Delta E_{ST} < 0.02$ eV. As a result, an efficient RISC channel ($T_1 \rightarrow S_{exc}$) with $k_{RISC} = 6.5 \times 10^5$ s^{-1} can be facilitated, leading to intrinsic TADF with τ_{DF} = 2.50 μs and Φ_{DF}/Φ_F = 0.37 in DCM solution. Through co-facial dimerization, we successfully converted a TADF-inactive chromophore (CzB, $k_{RISC} = 1.5 \times 10^4$ s^{-1}) into a TADF-active emitter (Np-2CzB, $k_{RISC} = 6.5 \times 10^5$ s^{-1}) with ~50 times promotion of k_{RISC}.

Conclusions

To summarize, we demonstrated a general strategy of molecular design, which can potentially facilitate the intrinsic TADF of

conjugated emitters with LE ($\pi \rightarrow \pi^*$) dominated S_1 and T_1 states. With a TADF-inactive B,N-MR emitter as a model system, we synthesized a co-facial dimer with suitable structure and electronic coupling, in which an excimer-like state (S_{exc}) was facilitated with ~250 ps formation time. Relying on enhanced SOC (S_{exc}–T_1) and reduced ΔE_{ST}, an intrinsic TADF with $k_{RISC} = 6.5 \times 10^5\ s^{-1}$ and $\Phi_{DF}/\Phi_F > 37\%$ was successfully demonstrated in dilute solution. Further investigation indicated that a suitable co-facial distance ($d = \sim 4.7$ Å) and inter-chromophore electronic coupling ($J_{coul} > 450\ cm^{-1}$) are essential for S_{exc} formation, while suppressing a key vibrational mode (CzB bending) can be critical to avoid disrupting the inter-chromophore interaction. For the majority of conjugated organic emitters, the lack of intrinsic TADF greatly limits their application in emerging areas such as OLED and EPOL devices. Although the present strategy was demonstrated with a B,N-MR emitter as a model system, we believe that it can be regarded as a general strategy for other types of organic emitter, as long as they feature a rigid conjugated framework and localized $\pi \rightarrow \pi^*$ character of S_1 and T_1 states. By activating the intrinsic DF emission, many traditional organic emitters might play more important roles in a wide range of applications, for which our work might provide inspiration for the community.

Data availability

The data supporting this article have been included as part of the ESI.†

Author contributions

Yixuan Gao: conceptualization, methodology, investigation, data curation, formal analysis, visualization, and writing – original draft; Yingman Sun: synthesis the compounds; Zilong Guo: investigation, visualization, project administration, and supervision; Guo Yu: participated in the discussion of the inter-chromophore interaction; Yaxin Wang: methodology, data curation, formal analysis, and validation; Yan Wan: methodology and resources; Yandong Han and Wensheng Yang: resources and project administration; Dongbing Zhao: supervision, resources, and funding acquisition; Xiaonan Ma: conceptualization, formal analysis, funding acquisition, supervision, and writing – review & editing.

Conflicts of interest

The authors declare no competing financial interest.

Acknowledgements

This work was supported by the National Key R&D Program of China (Grant No. 2020YFA0714603 and 2020YFA0714604). Y. G. is grateful to the Excellent Doctoral Thesis Cultivating Grant of Tianjin University. We thank Prof. Tao Xue (Analytical and Testing Centre of Tianjin University) for his valuable support on TCSPC measurements.

Notes and references

1 Y. Liu, C. Li, Z. Ren, S. Yan and M. R. Bryce, *Nat. Rev. Mater.*, 2018, **3**, 18020.
2 H. Uoyama, K. Goushi, K. Shizu, H. Nomura and C. Adachi, *Nature*, 2012, **492**, 234–238.
3 Z. Yang, Z. Mao, Z. Xie, Y. Zhang, S. Liu, J. Zhao, J. Xu, Z. Chi and M. P. Aldred, *Chem. Soc. Rev.*, 2017, **46**, 915–1016.
4 M. N. Berberan-Santos and J. M. M. Garcia, *J. Am. Chem. Soc.*, 1996, **118**, 9391–9394.
5 Z. Huang, D. Ji, A. Xia, F. Koberling, M. Patting and R. Erdmann, *J. Am. Chem. Soc.*, 2005, **127**, 8064–8066.
6 Q. Zhang, B. Li, S. Huang, H. Nomura, H. Tanaka and C. Adachi, *Nat. Photonics*, 2014, **8**, 326–332.
7 H. Kaji, H. Suzuki, T. Fukushima, K. Shizu, K. Suzuki, S. Kubo, T. Komino, H. Oiwa, F. Suzuki, A. Wakamiya, Y. Murata and C. Adachi, *Nat. Commun.*, 2015, **6**, 8476.
8 Z. Huang, B. Lei, D. Yang, D. Ma, Z. Bin and J. You, *Angew. Chem., Int. Ed.*, 2022, **134**, e202213157.
9 L. J. Rothberg and A. J. Lovinger, *J. Mater. Res.*, 1996, **11**, 3174–3187.
10 M. Pope, H. P. Kallmann and P. Magnante, *J. Chem. Phys.*, 1963, **38**, 2042–2043.
11 K. Goushi, K. Yoshida, K. Sato and C. Adachi, *Nat. Photonics*, 2012, **6**, 253–258.
12 M. A. Baldo, D. F. O'Brien, Y. You, A. Shoustikov, S. Sibley, M. E. Thompson and S. R. Forrest, *Nature*, 1998, **395**, 151–154.
13 D.-H. Kim, A. D'Aléo, X.-K. Chen, A. D. S. Sandanayaka, D. Yao, L. Zhao, T. Komino, E. Zaborova, G. Canard, Y. Tsuchiya, E. Choi, J. W. Wu, F. Fages, J.-L. Brédas, J.-C. Ribierre and C. Adachi, *Nat. Photonics*, 2018, **12**, 98–104.
14 A. J. C. Kuehne and M. C. Gather, *Chem. Rev.*, 2016, **116**, 12823–12864.
15 T. Zhang, Z. Zhou, X. Liu, K. Wang, Y. Fan, C. Zhang, J. Yao, Y. Yan and Y. S. Zhao, *J. Am. Chem. Soc.*, 2021, **143**, 20249–20255.
16 Z. Zhou, C. Qiao, K. Wang, L. Wang, J. Liang, Q. Peng, Z. Wei, H. Dong, C. Zhang, Z. Shuai, Y. Yan and Y. S. Zhao, *Angew. Chem., Int. Ed.*, 2020, **59**, 21677–21682.
17 N. R. Paisley, S. V. Halldorson, M. V. Tran, R. Gupta, S. Kamal, W. R. Algar and Z. M. Hudson, *Angew. Chem., Int. Ed.*, 2021, **60**, 18630–18638.
18 A. P. Demchenko, V. I. Tomin and P.-T. Chou, *Chem. Rev.*, 2017, **117**, 13353–13381.
19 G. Valenti, S. Scarabino, B. Goudeau, A. Lesch, M. Jović, E. Villani, M. Sentic, S. Rapino, S. Arbault, F. Paolucci and N. Sojic, *J. Am. Chem. Soc.*, 2017, **139**, 16830–16837.
20 D. M. Mayder, R. Hojo, W. L. Primrose, C. M. Tonge and Z. M. Hudson, *Adv. Funct. Mater.*, 2022, **32**, 2204087.
21 M. Zhao, M. Li, W. Li, S. Du, Z. Chen, M. Luo, Y. Qiu, X. Lu, S. Yang, Z. Wang, J. Zhang, S. Su and Z. Ge, *Angew. Chem., Int. Ed.*, 2022, **134**, e202210687.
22 C. J. Christopherson, N. R. Paisley, Z. Xiao, W. R. Algar and Z. M. Hudson, *J. Am. Chem. Soc.*, 2021, **143**, 13342–13349.

23 R. Englman and J. Jortner, *Mol. Phys.*, 1970, **18**, 145–164.
24 Y.-C. Wei, S. F. Wang, Y. Hu, L.-S. Liao, D.-G. Chen, K.-H. Chang, C.-W. Wang, S.-H. Liu, W.-H. Chan, J.-L. Liao, W.-Y. Hung, T.-H. Wang, P.-T. Chen, H.-F. Hsu, Y. Chi and P.-T. Chou, *Nat. Photonics*, 2020, **14**, 570–577.
25 Y. Wei, B. Chen, R. Ye, H. Huang, J. Su, C. Lin, J. Hodgkiss, L. Hsu, Y. Chi, K. Chen, C. Lu, S. Yang and P. Chou, *Angew. Chem., Int. Ed.*, 2023, **62**, e202300815.
26 G. Chen, J. R. Swartzfager and J. B. Asbury, *J. Am. Chem. Soc.*, 2023, **145**, 25495–25504.
27 V. Lawetz, G. Orlandi and W. Siebrand, *J. Chem. Phys.*, 1972, **56**, 4058–4072.
28 D. Beljonne, Z. Shuai, G. Pourtois and J. L. Bredas, *J. Phys. Chem. A*, 2001, **105**, 3899–3907.
29 T.-L. Wu, M.-J. Huang, C.-C. Lin, P.-Y. Huang, T.-Y. Chou, R.-W. Chen-Cheng, H.-W. Lin, R.-S. Liu and C.-H. Cheng, *Nat. Photonics*, 2018, **12**, 235–240.
30 H. Narita, H. Min, N. Kubo, I. Hattori, T. Yasuda and S. Yamaguchi, *Angew. Chem., Int. Ed.*, 2024, **63**, e202405412.
31 Y. Gao, Y. Wang, Z. Guo, Y. Wan, Z. Xue, Y. Han, W. Yang and X. Ma, *Chem. Sci.*, 2024, **15**, 6410–6420.
32 J. Gibson, A. P. Monkman and T. J. Penfold, *ChemPhysChem*, 2016, **17**, 2956–2961.
33 K. Stavrou, L. G. Franca, T. Böhmer, L. M. Duben, C. M. Marian and A. P. Monkman, *Adv. Funct. Mater.*, 2023, **33**, 2300910.
34 L. G. Franca, A. Danos, R. Saxena, S. Kuila, K. Stavrou, C. Li, S. Wedler, A. Köhler and A. P. Monkman, *J. Phys. Chem. Lett.*, 2024, **15**, 1734–1740.
35 A. K. Narsaria, F. Rauch, J. Krebs, P. Endres, A. Friedrich, I. Krummenacher, H. Braunschweig, M. Finze, J. Nitsch, F. M. Bickelhaupt and T. B. Marder, *Adv. Funct. Mater.*, 2020, **30**, 2002064.
36 H. Noda, X.-K. Chen, H. Nakanotani, T. Hosokai, M. Miyajima, N. Notsuka, Y. Kashima, J.-L. Brédas and C. Adachi, *Nat. Mater.*, 2019, **18**, 1084–1090.
37 Y.-Z. Shi, H. Wu, K. Wang, J. Yu, X.-M. Ou and X.-H. Zhang, *Chem. Sci.*, 2022, **13**, 3625–3651.
38 D. H. Ahn, S. W. Kim, H. Lee, I. J. Ko, D. Karthik, J. Y. Lee and J. H. Kwon, *Nat. Photonics*, 2019, **13**, 540–546.
39 G. Zhao, D. Liu, P. Wang, X. Huang, H. Chen, Y. Zhang, D. Zhang, W. Jiang, Y. Sun and L. Duan, *Angew. Chem., Int. Ed.*, 2022, **61**, e202212861.
40 Z. Cai, X. Wu, H. Liu, J. Guo, D. Yang, D. Ma, Z. Zhao and B. Z. Tang, *Angew. Chem., Int. Ed.*, 2021, **133**, 23827–23832.
41 S. Koseki, M. S. Gordon, M. W. Schmidt and N. Matsunaga, *J. Phys. Chem.*, 1995, **99**, 12764–12772.
42 S. Koseki, M. W. Schmidt and M. S. Gordon, *J. Phys. Chem. A*, 1998, **102**, 10430–10435.
43 T. J. Penfold, E. Gindensperger, C. Daniel and C. M. Marian, *Chem. Rev.*, 2018, **118**, 6975–7025.
44 W. Zhang, S. Li, Y. Gong, J. Zhang, Y. Zhou, J. Kong, H. Fu and M. Zhou, *Angew. Chem., Int. Ed.*, 2024, **63**, e202404978.
45 Y. Shi, H. Ma, Z. Sun, W. Zhao, G. Sun and Q. Peng, *Angew. Chem., Int. Ed.*, 2022, **61**, e202213463.
46 T. Hatakeyama, K. Shiren, K. Nakajima, S. Nomura, S. Nakatsuka, K. Kinoshita, J. Ni, Y. Ono and T. Ikuta, *Adv. Mater.*, 2016, **28**, 2777–2781.
47 B. Lei, Z. Huang, S. Li, J. Liu, Z. Bin and J. You, *Angew. Chem., Int. Ed.*, 2023, **62**, e202218405.
48 Y. Xu, Q. Wang, X. Cai, C. Li, S. Jiang and Y. Wang, *Angew. Chem., Int. Ed.*, 2023, **62**, e202312451.
49 X. Cai, Y. Pu, C. Li, Z. Wang and Y. Wang, *Angew. Chem., Int. Ed.*, 2023, **62**, e202304104.
50 Y. Wang, Y. Tian, Y. Gao, Z. Guo, Z. Xue, Y. Han, W. Yang and X. Ma, *J. Phys. Chem. Lett.*, 2023, **14**, 9665–9676.
51 P. Li, W. Li, Y. Zhang, P. Zhang, X. Wang, C. Yin and R. Chen, *ACS Mater. Lett.*, 2024, **6**, 1746–1768.
52 X. Cai, J. Xue, C. Li, B. Liang, A. Ying, Y. Tan, S. Gong and Y. Wang, *Angew. Chem., Int. Ed.*, 2022, **134**, e202200337.
53 H. Jiang, J. Jin and W. Wong, *Adv. Funct. Mater.*, 2023, **33**, 2306880.
54 Y. Zhang, D. Zhang, T. Huang, A. J. Gillett, Y. Liu, D. Hu, L. Cui, Z. Bin, G. Li, J. Wei and L. Duan, *Angew. Chem., Int. Ed.*, 2021, **60**, 20498–20503.
55 Y. Gao, Y. Wang, Z. Guo, Y. Wan, C. Li, B. Yang, W. Yang and X. Ma, *J. Phys. Chem. B*, 2022, **126**, 2729–2739.
56 J.-M. Teng, Y.-F. Wang and C.-F. Chen, *J. Mater. Chem. C*, 2020, **8**, 11340–11353.
57 X. Cao, K. Pan, J. Miao, X. Lv, Z. Huang, F. Ni, X. Yin, Y. Wei and C. Yang, *J. Am. Chem. Soc.*, 2022, **144**, 22976–22984.
58 Z. Chen, D. Liu, M. Li, Y. Jiao, Z. Yang, K. Liu and S. Su, *Adv. Funct. Mater.*, 2024, 2404278.
59 Y. X. Hu, J. Miao, T. Hua, Z. Huang, Y. Qi, Y. Zou, Y. Qiu, H. Xia, H. Liu, X. Cao and C. Yang, *Nat. Photonics*, 2022, **16**, 803–810.
60 Z. Huang, H. Xie, J. Miao, Y. Wei, Y. Zou, T. Hua, X. Cao and C. Yang, *J. Am. Chem. Soc.*, 2023, **145**, 12550–12560.
61 T. Xu, X. Liang and G. Xie, *Front. Chem.*, 2021, **9**, 691172.
62 X. Wu, B.-K. Su, D.-G. Chen, D. Liu, C.-C. Wu, Z.-X. Huang, T.-C. Lin, C.-H. Wu, M. Zhu, E. Y. Li, W.-Y. Hung, W. Zhu and P.-T. Chou, *Nat. Photonics*, 2021, **15**, 780–786.
63 J.-Y. Hu, Y.-J. Pu, G. Nakata, S. Kawata, H. Sasabe and J. Kido, *Chem. Commun.*, 2012, **48**, 8434.
64 D. Thirion, M. Romain, J. Rault-Berthelot and C. Poriel, *J. Mater. Chem.*, 2012, **22**, 7149.
65 J.-Y. Hu, Y.-J. Pu, Y. Yamashita, F. Satoh, S. Kawata, H. Katagiri, H. Sasabe and J. Kido, *J. Mater. Chem. C*, 2013, **1**, 3871.
66 Q. Liao, A. Li, A. Huang, J. Wang, K. Chang, H. Li, P. Yao, C. Zhong, P. Xie, J. Wang, Z. Li and Q. Li, *Chem. Sci.*, 2024, **15**, 4364–4373.
67 M. Yang, I. S. Park and T. Yasuda, *J. Am. Chem. Soc.*, 2020, **142**, 19468–19472.
68 S. Xu, Q. Yang, Y. Zhang, H. Li, Q. Xue, G. Xie, M. Gu, J. Jin, L. Huang and R. Chen, *Chin. Chem. Lett.*, 2021, **32**, 1372–1376.
69 E. Sebastian, J. Sunny and M. Hariharan, *Chem. Sci.*, 2022, **13**, 10824–10835.
70 M. P. Lijina, A. Benny, E. Sebastian and M. Hariharan, *Chem. Soc. Rev.*, 2023, **52**, 6664–6679.

71 P. Panthakkal Das, A. Mazumder, M. Rajeevan, R. S. Swathi and M. Hariharan, *Phys. Chem. Chem. Phys.*, 2024, **26**, 2007–2015.
72 Y. Hong, W. Kim, T. Kim, C. Kaufmann, H. Kim, F. Würthner and D. Kim, *Angew. Chem., Int. Ed.*, 2022, **61**, e202114474.
73 W. Guo, W. Zhao, K. Tan, M. Li and C. Chen, *Angew. Chem., Int. Ed.*, 2024, **63**, e202401835.
74 F. Zhang, F. Rauch, A. Swain, T. B. Marder and P. Ravat, *Angew. Chem., Int. Ed.*, 2023, **62**, e202218965.
75 J.-K. Li, X.-Y. Chen, Y.-L. Guo, X.-C. Wang, A. C.-H. Sue, X.-Y. Cao and X.-Y. Wang, *J. Am. Chem. Soc.*, 2021, **143**, 17958–17963.
76 G. Jones, W. R. Jackson, C. Y. Choi and W. R. Bergmark, *J. Phys. Chem.*, 1985, **89**, 294–300.
77 F. Würthner, C. R. Saha-Möller, B. Fimmel, S. Ogi, P. Leowanawat and D. Schmidt, *Chem. Rev.*, 2016, **116**, 962–1052.
78 A. G. Crawford, A. D. Dwyer, Z. Liu, A. Steffen, A. Beeby, L.-O. Pålsson, D. J. Tozer and T. B. Marder, *J. Am. Chem. Soc.*, 2011, **133**, 13349–13362.
79 C.-W. Ju, B. Li, L. Li, W. Yan, C. Cui, X. Ma and D. Zhao, *J. Am. Chem. Soc.*, 2021, **143**, 5903–5916.
80 U. Müller, L. Roos, M. Frank, M. Deutsch, S. Hammer, M. Krumrein, A. Friedrich, T. B. Marder, B. Engels, A. Krueger and J. Pflaum, *J. Phys. Chem. C*, 2020, **124**, 19435–19446.
81 R. Jing, Y. Li, K. Tajima, Y. Wan, N. Fukui, H. Shinokubo, Z. Kuang and A. Xia, *J. Phys. Chem. Lett.*, 2024, **15**, 1469–1476.
82 P. Roy, G. Bressan, J. Gretton, A. N. Cammidge and S. R. Meech, *Angew. Chem., Int. Ed.*, 2021, **60**, 10568–10572.
83 Y. Wang, Z. Guo, Y. Gao, Y. Tian, Y. Deng, X. Ma and W. Yang, *J. Phys. Chem. Lett.*, 2022, **13**, 6664–6673.
84 M. Y. Wong and E. Zysman-Colman, *Adv. Mater.*, 2017, **29**, 1605444.
85 T. Azumi, A. T. Armstrong and S. P. McGlynn, *J. Chem. Phys.*, 1964, **41**, 3839–3852.
86 R. M. Young and M. R. Wasielewski, *Acc. Chem. Res.*, 2020, **53**, 1957–1968.
87 F. M. Winnik, *Chem. Rev.*, 1993, **93**, 587–614.
88 N. J. Hestand and F. C. Spano, *J. Chem. Phys.*, 2015, **143**, 244707.
89 S. Kang, T. Kim, Y. Hong, F. Würthner and D. Kim, *J. Am. Chem. Soc.*, 2021, **143**, 9825–9833.
90 D. Bialas, E. Kirchner, M. I. S. Röhr and F. Würthner, *J. Am. Chem. Soc.*, 2021, **143**, 4500–4518.
91 N. J. Hestand and F. C. Spano, *Chem. Rev.*, 2018, **118**, 7069–7163.
92 M. Kasha, H. R. Rawls and M. Ashraf El-Bayoumi, *Pure Appl. Chem.*, 1965, **11**, 371–392.
93 C. Lin, T. Kim, J. D. Schultz, R. M. Young and M. R. Wasielewski, *Nat. Chem.*, 2022, **14**, 786–793.
94 E. Sebastian and M. Hariharan, *J. Am. Chem. Soc.*, 2021, **143**, 13769–13781.
95 C. Kaufmann, D. Bialas, M. Stolte and F. Würthner, *J. Am. Chem. Soc.*, 2018, **140**, 9986–9995.
96 Y. Hong, J. Kim, W. Kim, C. Kaufmann, H. Kim, F. Würthner and D. Kim, *J. Am. Chem. Soc.*, 2020, **142**, 7845–7857.
97 X. Qiu, G. Tian, C. Lin, Y. Pan, X. Ye, B. Wang, D. Ma, D. Hu, Y. Luo and Y. Ma, *Adv. Opt. Mater.*, 2021, **9**, 2001845.
98 Z. Wang, R. Jing, Y. Li, D. Song, Y. Wan, N. Fukui, H. Shinokubo, Z. Kuang and A. Xia, *J. Phys. Chem. Lett.*, 2023, **14**, 8485–8492.
99 H.-M. Pan, C.-C. Wu, C.-Y. Lin, C.-S. Hsu, Y.-C. Tsai, P. Chowdhury, C.-H. Wang, K.-H. Chang, C.-H. Yang, M.-H. Liu, Y.-C. Chen, S.-P. Su, Y.-J. Lee, H. K. Chiang, Y.-H. Chan and P.-T. Chou, *J. Am. Chem. Soc.*, 2023, **145**, 516–526.
100 S. Jiang, Y. Yu, D. Li, Z. Chen, Y. He, M. Li, G. Yang, W. Qiu, Z. Yang, Y. Gan, J. Lin, Y. Ma and S. Su, *Angew. Chem., Int. Ed.*, 2023, **62**, e202218892.
101 H. Masuhara, N. Tamai, N. Mataga, F. C. De Schryver and J. Vandendriessche, *J. Am. Chem. Soc.*, 1983, **105**, 7256–7262.
102 T. Karatsu, T. Shibata, A. Nishigaki, A. Kitamura, Y. Hatanaka, Y. Nishimura, S. Sato and I. Yamazaki, *J. Phys. Chem. B*, 2003, **107**, 12184–12191.